Large-Eddy Simulation and Challenges for Projection-based Reduced-Order Modeling of a Gas Turbine Model Combustor

Symposium on Thermoacoustics in Combustion: Industry meets Academia (SoTiC 2021)
Sept. 6 - Sept. 10, 2021
Munich, Germany
Paper No.: 8475

Nicholas Arnold-Medabalimi[1], Cheng Huang[2], and Karthik Duraisamy[1]

Abstract

Computationally efficient modeling of gas turbine combustion is challenging due to the chaotic multi-scale physics and the complex non-linear interactions between acoustic, hydrodynamic, and chemical processes. A large-eddy simulation (LES) is conducted for the model combustor of Meier et al. (1) using an unstructured mesh finite volume method with turbulent combustion effects modeled using a flamelet-based method. The flow field is validated via comparison to averaged and unsteady high-frequency particle image velocimetry (PIV) fields. A high degree of correlation is noted with the experiment in terms of flow field snapshots and via modal analysis. The dynamics of the precessing vortex core (PVC) is quantitatively characterized using dynamic mode decomposition. The validated FOM dataset is used to construct projection-based ROMs, which aim to reduce the system dimension by projecting the state onto a reduced dimensional linear manifold. The use of a structure-preserving least squares formulation (SP-LSVT) guarantees stability of the ROM, compared to traditional model reduction techniques. The SP-LSVT ROM provides accurate reconstruction of the combustion dynamics within the training region, but faces a significant challenge in future state predictions. This limitation is mainly due to the increased projection error, which in turn is a direct consequence of the highly chaotic nature of the flow field, involving a wide range of disperse coherent structures. Formal projection-based ROMs have not been applied to a problem of this scale and complexity, and achieving accurate and efficient ROMs is a grand challenge problem. Further advances in non-linear manifold projections or adaptive basis projections have the potential to improve the predictive capability of this class of ROMs.

Keywords

Computational Fluid Dynamics; Gas Turbine Dynamics; Reduced-Order Modeling

Introduction

Over the past two decades, the requirements on newly-developed combustion devices have increased significantly (2). The aviation industry has actively pursued improved performance (e.g., fuel efficiency) and reduced emissions. On the other hand, for power generation applications, the design of gas turbines incorporates additional requirements. The modern power generation landscape has made traditional combustion power generation profitable on a day-to-day and even hour-to-hour basis. This variability in demand is due to improved energy efficiencies and diversification of power generation sources, most notably renewable sources. These considerations economically incentivize traditional gas-turbine energy systems to have the capability to operate at specific power levels and quickly adjust output to satisfy different power grid demands while maintaining profitability.

To accommodate these three requirements, namely improved efficiency, reduced emissions, and operational flexibility, the gas turbine combustor is usually designed to operate at fuel-lean conditions, which makes it more susceptible to undesirable phenomena, most notably combustion instability. The coupling between chemical reactions and acoustic waves can significantly affect device performance. Previous designs have leveraged physical adjustments to promote passive stability (3) as well as active control (4) at the *design point* to damp these harmful effects, but dynamic operation adds the extra challenge of maintaining stability at multiple operating points.

Combustion instability (or thermoacoustic instability) has remained an area of significant concern in combustion device design. This phenomenon is characterized by large-amplitude pressure oscillations, which can lead to catastrophic device failure. The primary mechanism of combustion instability can be attributed to the interactions between flow dynamics, acoustics, and chemical reactions. The observation of this phenomenon has been documented by Mallard and Le Chatelier (5). Lord Rayleigh (6) proposed an elegant explanation for combustion instability based on the phase relationship between unsteady acoustics and chemical reactions (or, more precisely, the pressure and heat release fluctuations). However, in real combustion devices, the occurrence of combustion instability can be influenced by many factors, including geometric details, operating

[1]University of Michigan, USA [2]University of Kansas, USA

Corresponding author:
Nicholas Arnold-Medabalimi, University of Michigan Department of Aerospace Engineering, Ann Arbor, MI 48105 USA
Email: narnoldm@umich.edu

conditions, and propellants. This also introduces additional challenges in developing predictive models. With recent advances in computational modeling, detailed simulations can be used to investigate the mechanisms of combustion instability for complex geometries. Especially, Large-Eddy Simulation (LES) have the potential to provide valuable insight into the underlying unsteady dynamics. Huang et al. (7; 8; 9) applied LES to a standard lean-premixed (LP) combustor (10). Since these initial investigations, LES techniques have advanced as a modeling tool in combustion instability-prone systems. Within gas turbine-type systems, these simulation studies have been applied to a variety of problems ranging from laboratory combustors for both atmospheric (11) and high-pressure (12) conditions to (albeit under-resolved) studies of large-scale practical gas turbines (13).

Gas Turbine Model Combustors : Experiments & Simulations

Gas turbine model combustors (GTMCs) have been developed to enhance the understanding of the underlying physics inherent to practical gas turbine systems in a laboratory environment and act as validation cases for developing modeling capabilities. These laboratory burners have spanned a range of different geometries, injection schemes, and stabilization strategies. A comprehensive collection of a variety of different GTMC experimental configurations can be found in Stohr et al. (14). Of particular note are the family of burners being studied at the German Aerospace Center (Deutsches Zentrum für Luft-und Raumfaht(DLR)). These have included the PRECCINSTA burner (15), the dual-swirl burner (16; 17; 1), and most recently the independent dual-swirl burner (18; 19; 20).

In the present work, focus is placed on the DLR dual-swirl burner developed by Meier et al. (1; 16) This burner deviates from previous designs by virtue of having multiple swirlers and a partially premixed combustion regime. The dual swirl burner is characterized by three distinct operating conditions referenced as flame A, B, and C. Flame A exhibited a stable V-shaped flame, while flame B operated as an unstable flat flame with peak instability at 280-300 Hz. Finally, flame C operated near the flammability limits with periodic blowout and re-ignition observed. These conditions have been examined using both stereoscopic particle image velocimetry (stereo-PIV), Raman spectroscopy, OH*/CH* chemiluminescence, and OH/CH/CH2O planar laser-induced fluorescence (PLIF). These measurements were used to characterize both the steady and unsteady performance of the burner. Studies included swirl number dependencies, flow structure development (21), precessing vortex core behavior (22), unsteady local mixing (23), and vortex flame interaction (14). In addition to the original work conducted by DLR, an identical setup was investigated by Allison et al. (24; 25) which focused on the behavior of the burner when operating at various equivalence ratios and particularly with more complex fuels, most notably syngas.

In concert with these experimental measurements, a variety of modeling efforts have been attempted on this geometry. To the knowledge of the authors, the first attempt was the work of Widenhorn et al. (26) which simulated the whole geometry under the flame A conditions and showed reasonable average velocity field comparison. A more comprehensive modeling effort was conducted by See and Ihme (11) who used a modified flamelet model, and showed good agreement in the flame A averaged field condition. Additional work by Koo et al. (27) focused on accurate modeling of soot formation in the system. These works primarily focused on the turbulent combustion modeling of the stable flame A configuration, focusing on flamelet model augmentation and particulate matter generation, respectively. Recent work by Chen et al. (28; 29) comprehensively modeled both the flame A and B conditions with a focus on the instability as well as validation of both the stable and unstable flame operating conditions representing the first complete steady and unsteady modeling of this system.

Reduced-Order Modeling

Though LES is becoming affordable for complex problems and can reveal details of the underlying physics that are inaccessible through experiment, these techniques are still far out-of-reach for use in many-query applications (e.g., design, optimization, and uncertainty quantification). Therefore, it is imperative to develop reduced models that can inherit the fidelity of the LES, while being much more efficient for many-query computations. One class of these methods is the projection-based reduced-order model (ROM), which attempts to develop a dynamical system with reduced-dimension to represent the full-order model (FOM) (e.g., LES). These methods have been proven effective in reducing the dynamics for flow control (30; 31; 32). However, when applied to multi-scale problems containing transport phenomena such as convection, projection-based ROMs suffer in both accuracy and stability. These shortcomings can arise from a combination of numerical stability of the projection (e.g. Galerkin (33)), the truncation of low-energy modes (34), and the inefficiency of linear manifolds in representing convective phenomena (35).

Several strategies have been suggested to mitigate these challenges. Balanced proper orthogonal decomposition has been used in linear systems to form stable ROMs (36; 37). Attempts have also been made to improve ROM stability via examination of the underlying numerical discretization through various methods. Rowley et al.(38) ensured that the computed inner product for the Galerkin projection is physically meaningful. Parish et al. (39) used the Mori-Zwanzig formalism to develop a Petrov-Galerkin-type closure. Ahmed et al. (40) present a comprehensive review of the state of the art in closure modeling for projection-based ROMs. It has been shown that maintaining the conservation properties of the governing equations is critical in ROM development (41). A method demonstrated by (42) generates stable non-linear ROMs by minimizing the least-squares residual of the projected solution, yielding in a symmetrized and linearly stable ROM. This popular method is referred to as the least-squares Petrov Galerkin (LSPG) method.

In the context of reacting flow simulations, several additional challenges arise. A key challenge in computational combustion has been the numerical stiffness inherent to kinetics. When modeled using ROM methods, spurious

oscillations have been observed near the high gradient conditions present in a flame front. These oscillations commonly lead to non-physical features such as negative temperature. Physical constraints have been applied to promote local stability with success.

The structure-preserving least-squares projection with variable transformation (SP-LVST) (43) is a ROM formulation specific to allow conservation to be maintained while using alternate variables. This change of variables is beneficial in the reacting flow context as using primitive variables (pressure, temperature, velocity) allows for simplified state calculations compared with conserved forms (density, enthalpy, momentum). This transformation is combined with least squares (to improve global stability), physical constraints (to improve local stability), and hyper-reduction methods (to achieve computational speed-up).

These developments have significantly increase the accuracy and robustness of the family of projection-based ROMs. However, all these techniques fundamentally operate by projecting a high dimensional system onto a reduced manifold. As a result the choice of the reduced space is just as significant in ROM development. The most common technique to develop the linear manifold is to use proper orthogonal decomposition (44) based on snapshots of the full state vector. Generally speaking, problems with a strong limit cycle coherence have seen success when compared with chaotic problems with limited magnitude coherence (45).

In this work, the flame A configuration of the DLR dual-swirl burner is simulated using flamelet-based Large-Eddy Simulations (LES). The simulations results are validated using experimental measurements. Following this, reduced-order modeling techniques are applied.

Methods

Governing Equations

Favre-averaging $\widetilde{\phi(x_i,t)}$ is used for velocity u, enthalpy h, total enthalpy h^0, temperature T, and the flamelet transport scalars Z_m, Z_v, C defined as

$$\widetilde{\phi(x_i,t)} = \frac{\langle \rho(x_i,t)\phi(x_i,t)\rangle}{\langle \rho(x_i,t)\rangle}$$

where the mean quantities $\langle\phi\rangle$ are defined by ,

$$\langle \phi(x_i,t)\rangle = \frac{1}{\Delta t}\int_t^{t+\Delta t} \phi(x_i,t')dt'.$$

The continuity and conservation of momentum and total enthalpy equations take the form of

$$\frac{\partial\langle\rho\rangle}{\partial t} + \frac{\partial\langle\rho\rangle\widetilde{u}_j}{\partial x_j} = 0.$$

$$\frac{\partial\langle\rho\rangle\widetilde{u}_i}{\partial t} + \frac{\partial\langle\rho\rangle\widetilde{u}_j\widetilde{u}_i}{\partial x_j} + \frac{\partial\langle p\rangle}{\partial x_i} - \frac{\partial\left(\widetilde{\tau_{ij}} - \widetilde{u_i''u_j''}\right)}{\partial x_j} = 0,$$

$$\begin{aligned}\frac{\partial(\langle\rho\rangle\widetilde{h^0} - \langle p\rangle)}{\partial t} + \frac{\partial\langle\rho\rangle\widetilde{u}_j\widetilde{h^0}}{\partial x_j} - \frac{\partial\widetilde{u}_i\widetilde{\tau_{ij}}}{\partial x_j} - \frac{\partial}{\partial x_j}\left(\lambda\frac{\partial\widetilde{T}}{\partial x_j}\right)\\ -\frac{\partial}{\partial x_j}\left(\langle\rho\rangle\sum_{l=1}^{N}\left[\langle h_l\rangle D_{lM}\frac{\partial\widetilde{Y_l}}{\partial x_j}\right]\right)\\ +\frac{\partial\widetilde{u}_i\widetilde{u_i''u_j''}}{\partial x_j} - \frac{\partial\langle\rho\rangle\widetilde{u_j''e''}}{\partial x_j} = 0.\end{aligned}$$

λ is the mixture heat transfer coefficient; D_{lM} is the diffusion coefficient of species l into the mixture M. Despite using a flamelet-based model, thermal transport quantities are calculated online based on the species compositions provided by the flamelet table. $\widetilde{\tau}_{ij}$ is the resolved viscous stress tensor assuming Newtonian fluid taking the form

$$\widetilde{\tau_{ij}} = 2\mu\widetilde{\epsilon}_{ij},$$

where

$$\widetilde{\epsilon}_{ij} = \left(\frac{1}{2}\left(\frac{\partial\widetilde{u}_i}{\partial x_j} + \frac{\partial\widetilde{u}_j}{\partial x_i}\right) - \frac{1}{3}\frac{\partial\widetilde{u}_k}{\partial\widetilde{u}_k}\delta_{ij}\right),$$

with the bulk viscosity neglected. $\widetilde{u_i''u_j''}$ is the large-eddy simulation(LES) mean stress modeled using the Nicoud Sigma model (46),

$$\widetilde{u_i''u_j''} = \tau_{ij}^{SGS} - \frac{1}{3}\tau_{kk}^{SGS}\delta_{ij} = 2\langle\rho\rangle\nu_t\widetilde{\epsilon}_{ij},$$

where the Leonard and cross-terms are neglected (47). The sub-grid scale turbulent viscosity is modeled as

$$\nu_t = (C_\sigma\Delta)^2\mathcal{D}_\sigma(\widetilde{u}),$$

where $\mathcal{D}_\sigma(\widetilde{u}) = \frac{\sigma_3(\sigma_1-\sigma_2)(\sigma_2-\sigma_3)}{\sigma_1^2}$. Here σ_i are the singular values of the resolved velocity gradient ordered greatest to least and Δ is the local cell size. The differential operator defines the subgrid-scale viscosity based on the singular values of the velocity gradient tensor ($\widetilde{g}_{ij} = \frac{\partial\widetilde{u}_i}{\partial\widetilde{x}_j}$). This model has been applied to other stabilized flame cases (48; 49) and has shown favorable comparison for the relatively small computation cost particularly in comparison to transport equation based models.

The enthalpy equation unresolved term is closed using the gradient-diffusion model using the turbulent viscosity and a turbulent Prandtl number Pr_t approximated as 0.7;

$$\widetilde{u_j''e''} = \frac{\nu_t}{Pr_t}\frac{\partial\widetilde{h}}{\partial x_j}$$

Turbulent Combustion Modeling

For this work, the flamelet progress variable approach (50)(FPVA) model was utilized. Instead of n species equations, 3 scalar equations are used to represent the Favre-filtered mean mixture fraction Z_m, mixture fraction variance Z''^2, and progress variable C.

$$\frac{\partial\langle\rho\rangle\widetilde{Z_m}}{\partial t} + \frac{\partial\langle\rho\rangle\widetilde{u}_j\widetilde{Z_m}}{\partial x_j} - \frac{\partial}{\partial x_j}\langle\rho\rangle\left(D + \frac{\nu_t}{Sc_t}\right)\frac{\partial\widetilde{Z_m}}{\partial x_j} = 0$$

$$\begin{aligned}\frac{\partial\langle\rho\rangle\widetilde{Z''^2}}{\partial t} + \frac{\partial\langle\rho\rangle\widetilde{u}_j\widetilde{Z''^2}}{\partial x_j} - \frac{\partial}{\partial x_j}\langle\rho\rangle\left(D + \frac{\nu_t}{Sc_t}\right)\frac{\partial\widetilde{Z''^2}}{\partial x_j} =\\ 2\langle\rho\rangle\Big(\underbrace{\frac{\nu_t}{Sc_t}\frac{\partial\widetilde{Z_m}}{\partial x_j}\frac{\partial\widetilde{Z_m}}{\partial x_j}}_{Production} - \underbrace{C_Z\frac{\nu_t}{\Delta^2}\widetilde{Z''^2}}_{Dissipation}\Big)\end{aligned}$$

$$\frac{\partial\langle\rho\rangle\widetilde{C}}{\partial t}+\frac{\partial\langle\rho\rangle\widetilde{u}_j\widetilde{C}}{\partial x_j}-\frac{\partial}{\partial x_j}\langle\rho\rangle\big(D+\frac{\nu_t}{Sc_t}\big)\frac{\partial\widetilde{C}}{\partial x_j}=\langle\rho\rangle\widetilde{\dot{\omega}}_C,$$

where Sc_t is the turbulent Schmidt number, approximated as 0.7. The individual flamelets were generated using FlameMaster (51) using the GRI-12 mechanism (52). The flamelets were organized into a table for online computation with an adaptive mesh in the reaction zone. In traditional flamelet-based methods, all thermo-chemical and transport properties are interpolated from the generated look-up table at run time. In this work, only the species mass fractions are updated from the flamelet manifold. Because of the formulation of the energy equation in total enthalpy form, the resultant temperature and transport properties are recomputed using the species. The model maintains energy conservation but requires the computation of transport and thermodynamic properties from the local species composition and total enthalpy. The thermodynamic quantities are computed using the polynomials temperature relations of McBride (53), and the transport properties are computed using the mixing rules of Wilke (54) and Mathur (55) for viscosity and thermal conductivity, respectively.

Experimental Geometry

The burner configuration is shown in Fig. 1. The setup consists primarily of a combustion chamber with a square cross-section connected to a single plenum via a fixed dual swirler assembly. Dry atmospheric air is fed to the lower cylindrical plenum. The two swirlers are fed by this common plenum with symmetric piping to the upper swirler. The lower swirler feeds into a central converging nozzle (Diameter of 15mm at nozzle termination), while the upper swirler feeds a co-annular diverging section (Outer diameter 25mm, Inner Diameter 17mm at burner face). The outer annular section smoothly contours to the bottom plane of the combustion chamber. Un-swirled methane fuel is injected between the two swirled air streams co-axially. The fuel injection ports are formed by the stacking of the two swirler plates and are fed by three radial fuel lines. The central nozzle terminates 4.5 mm below the burner face. The combustion chamber is composed of a square cross-section (85^2 mm) with chamfered post corners with a total height of 110 mm. The chamber terminates by contracting to a cylindrical chimney (40mm diameter), opening to the laboratory atmosphere. The walls in the experimental setup are quartz to allow for optical access with substitute walls with mounted probes.

In the scope of this work, we focus on the 'flame A' conditions for FOM validation and the ROM methods being developed on this condition. For this configuration, the mass flow of air $\dot{m}_{air}$ is 1905 grams per minute, and the fuel inflow rate $\dot{m}_{fuel}$ is 41.8 grams per minute.

Computations

The Large-Eddy Simulations (LES) were conducted using an in-house CFD code, the General Equations and Mesh Solver (GEMS) (56). GEMS is a message passing interface (MPI)-based parallel, second-order accurate in time and space finite volume solver. An implicit dual time-stepping scheme is used, with Roe fluxes (57) and the Barth-Jespersen flux limiter (58). The numerical robustness of the solver allows for the resolution of near-wall flow features while using high aspect ratio grids. The simulation was conducted on Engineer Research and Development Center (ERDC) Onyx on 2200 cores. Each Onyx node is composed of two 22 core Intel E5-2699v4 Broadwell processors for a total of 44 cores with 128 GBytes per node running on the Cray Aries interconnect. Both cases were run with a physical time-step of one microsecond. The flame A simulation was run for a total of 200 milli-seconds of real-time, accounting for approximately two hundred characteristic flow through periods of the combustion chamber or 70 periods for the entire domain. The approximate wall-time per flow through period of the combustion chamber was two hours.

Computational Domain The mesh is composed of a fully structured multi-block topology with 7.5 million hexahedral cells. The computational domain is shown in Fig 4. The lowest minimum angle of hex elements is 24 degrees and is limited by the geometry (the angle at which the lower swirler vanes intersect with the core nozzle). Finally, the point spacing was allowed to vary to limit the lowest quality elements to areas where reactions do not occur, such as the plenum or upper combustion chamber and chimney. As shown by previous works (28; 11) the modeling of both the swirling vanes as well as air plenum of the combustor is critical for accurate prediction. Because of this, the entire combustor geometry is modeled. The only significant geometric modeling simplification was the fuel injection nozzle. The 72 individual fuel injector holes were approximated as a circular slot with a matching area to accommodate the structured mesh (Fig. 3). The air and fuel inflow conditions were specified to match the experimental mass flow. In systems utilizing swirler vanes, it is predicted that the swirler geometry generates nearly all of the significant turbulence. With this consideration, both inlets were specified as uniform velocities. The entire fuel plenum consists of 3 feed lines arranged radially (Fig. 1). These were not fully meshed, and instead, the fuel boundary condition sits recessed from the approximated slot. The outflow boundary condition was specified as a constant pressure set to atmospheric conditions. The wall boundaries were set to be adiabatic with an enforced no-slip condition.

The overall mesh topology focused on clustering cells in the lower combustion chamber. The minimum mesh spacing of $\Delta = .1$mm was constrained by the smallest feature of the system, the fuel injector, resulting in ten cells across the fuel injector ports (Fig. 3). A snapshot of the resulting mesh Δ is shown Fig. 4. Fine cells are clustered in the nozzle and lower combustion chamber regions. Because of the requirements of multi-block meshing and a desire to optimize computational cost, there are some locations with relatively coarse cells. However, these are limited to the upper corners of the combustion chamber, chimney, and lower plenum.

Full-Order Model (FOM) Results

In this section, the simulation results of the flame A condition for the GTMC dual-swirl burner with validation against experimental results will be described.

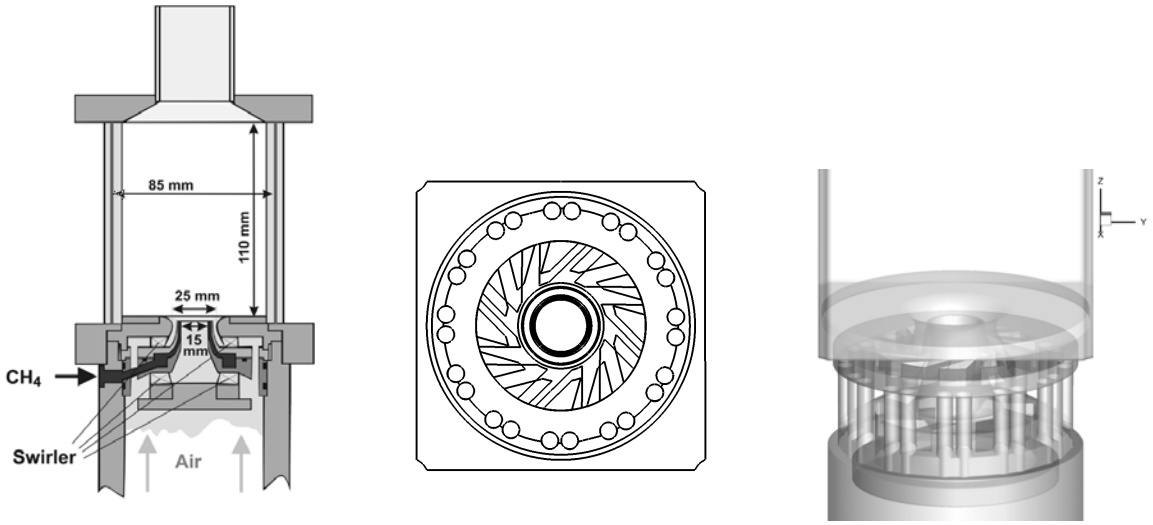

Figure 1. Burner schematic (17) (Left), stacked internal cutaway of swirler geometry(Center), and external iso-surface (Right)

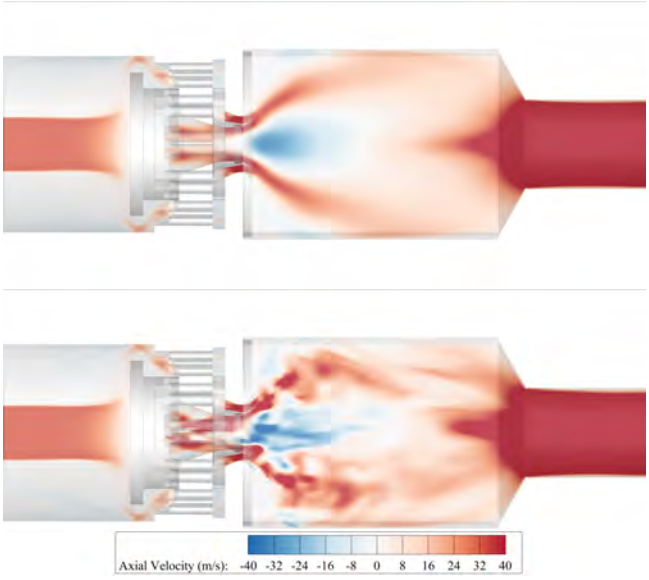

Figure 2. Representative averaged (Top) and instantaneous (Bottom) axial velocity fields for the flame A configuration

Averaged Velocity Field

The time and root mean square (RMS) averaged velocity fields are examined as an initial comparison between the simulation and experiment. A set of unsteady time realizations, representing 100 characteristic flow-through periods, were used to compute the cell-wise RMS and time averages. The resulting flow-fields are displayed for axial (Fig. 5), radial (Figs. 6), and swirl velocity (Figs. 7) with the corresponding experimental PIV measurement layered on the upper half of the contour. For a quantitative comparison, profiles are extracted for the experimental and computational data sets at various axial heights.

The overall structure is observed in all three dimensions with two areas of discrepancy. These variations are most observable in the axial velocity (Fig. 5 which has a contour line placed at the axial stagnation velocity). The first is the modeled height of the inner recirculating zone (IRZ), predicted at 4 mm lower than found experimentally.

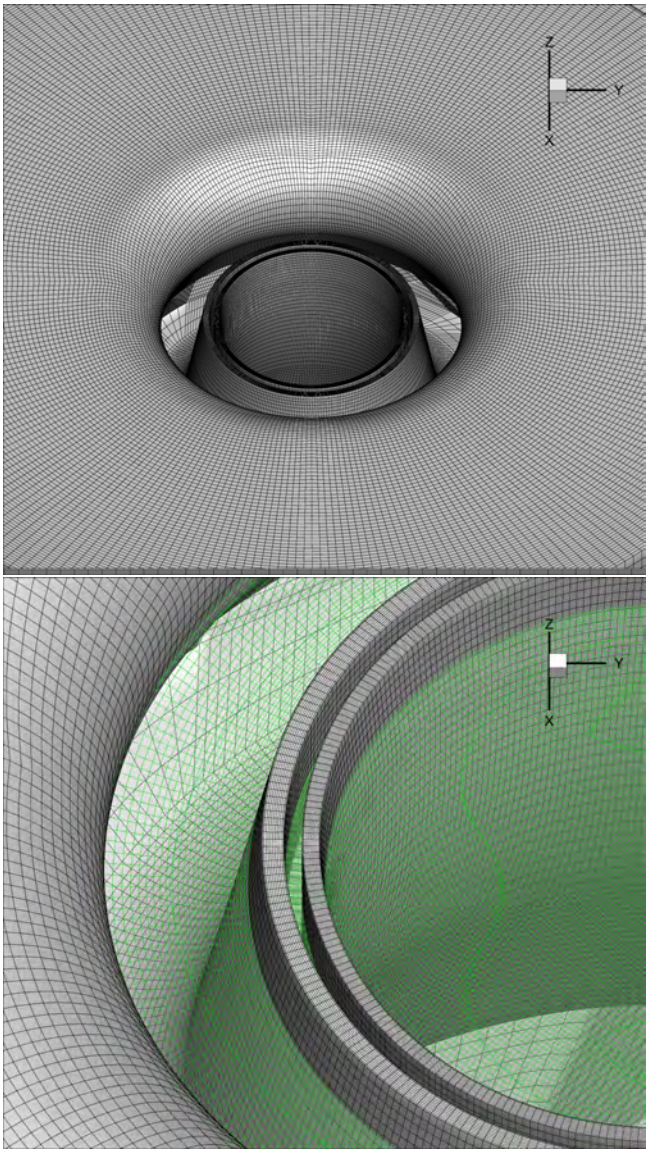

Figure 3. Fuel injection detail (Top) and internal cell spacing at injector face shown in green (Bottom)

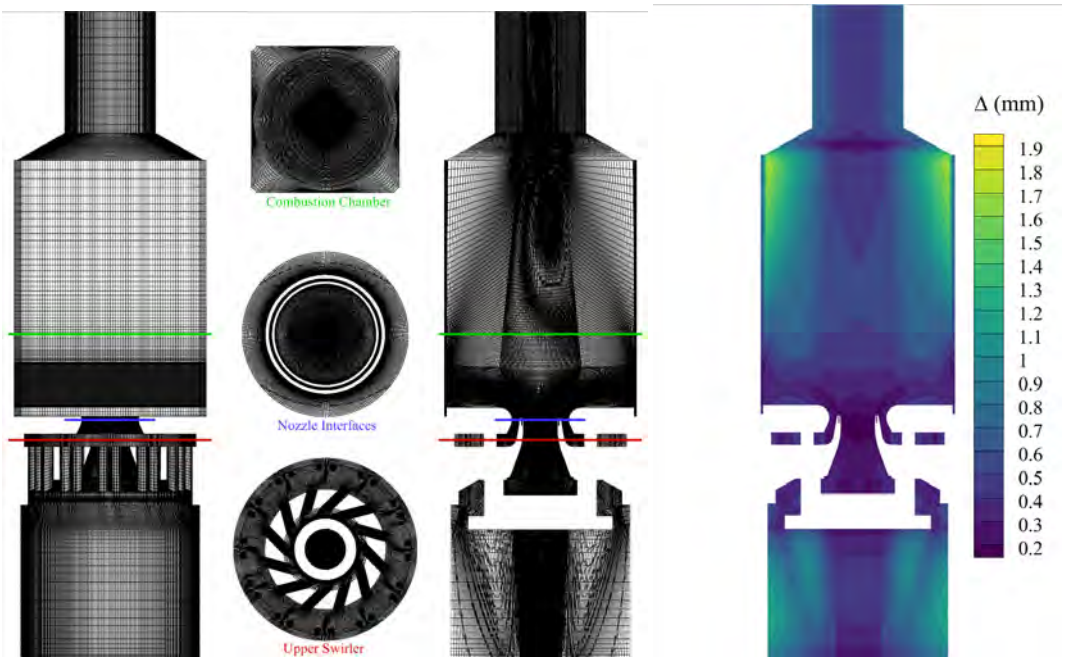

Figure 4. Mesh schematic with selected slice locations (Left) Mesh mean filter width slice (Right)

This height difference can be observed qualitatively from the contour and quantitatively in the $h = 1$mm profile near the center-line. This underprediction is expected in swirl stabilized flows and is consistent with previous computational studies (28). This characteristic is due to inadequate wall modeling near the nozzle termination. The second deviation is the prediction of the tail-like structure of the recirculation bubble. In works focused on modeling a vortex breakdown structure, a significantly finer mesh resolution is required. Interestingly, despite not correctly capturing the double tail structure of the recirculation bubble, the center-line stagnation point matches the experimental observations. Examining the extracted profiles, one can observe strong agreement in both time, and RMS-averaged quantities. Generally, because of the lower and smaller recirculation bubble, velocities were computed as lower than experimental values in the near nozzle region and overestimating in the combustor's upper region. Finally, the outer recirculation zones (ORZ), the recirculation zone in the lower outer corners of the chamber, are predicted accurately compared with the experimental values' size, shape, and magnitude.

A majority of the observations in the axial velocity hold when examining the corresponding radial(Fig. 6) and tangential(Fig. 7) velocity fields. Both time and RMS-averaged quantities correlate favorably with a relatively minor discrepancy in the average radial velocity profile peak, which persists in all near-nozzle profiles. This is expected to be due to inadequate wall spacing of the diverging nozzle section leading to an underestimation of the radial velocity measurements due to the slightly slimmer inner recirculation bubble.

Averaged Temperature and Mixture Fraction

For the dual-swirl GTMC, flame A corresponds to an acoustically broadband stable V-shaped flame. The mid-plane contours from the flame A case is shown in Fig. 8 along

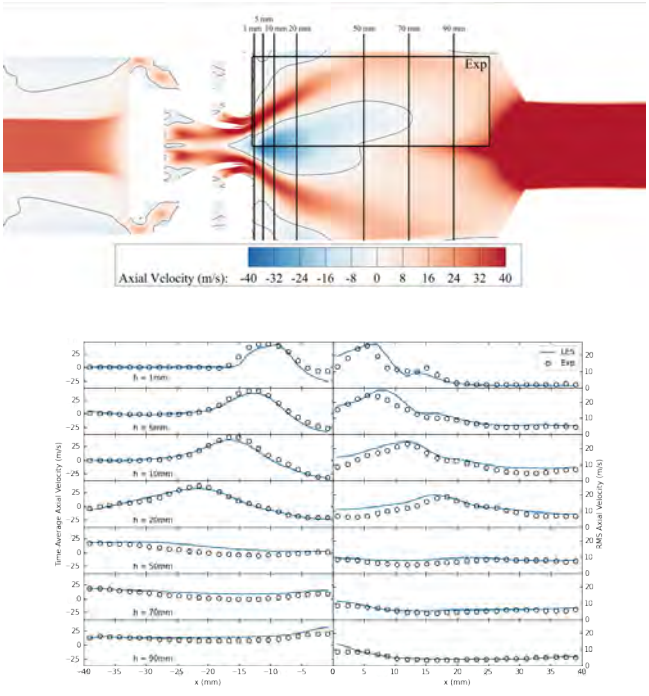

Figure 5. Time and RMS-averaged axial velocity comparisons of Flame A: experimental data superimposed on upper half of combustor with lines at Axial Velocity equal to zero

with extracted profiles from the simulation data compared with experimental measurements. We should note that the experimental spectroscopy values are spatially averaged, which can produce deviations compared with CFD filtered quantities. Qualitatively, flame A shows the characteristic V-shaped structure and compares well with the experimental profiles. A caveat is that the height of the flame, like the IRZ, is underpredicted. This underprediction can be observed in the relative overprediction in temperature near the burner

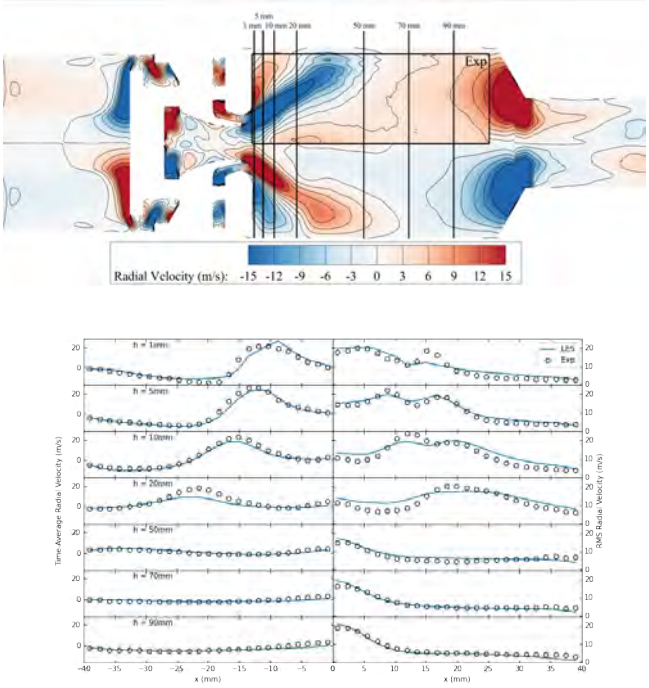

Figure 6. Time and RMS-averaged radial velocity of flame A

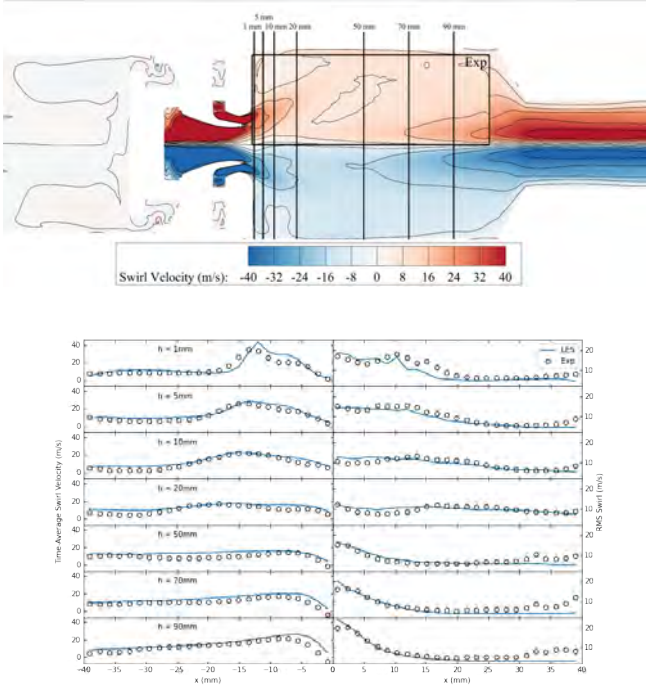

Figure 7. Time and RMS-averaged tangential velocity of flame A

face. This under-prediction is most likely a combination of the nozzle wall modeling, adiabatic wall boundary conditions, and partially premixed reactions. However, the overall characteristics of the temperature field are well captured.

Mixture Fraction Temperature Correlation

The Flamelet Progress Variable (FPVA) model does not have additional source terms to account for partially

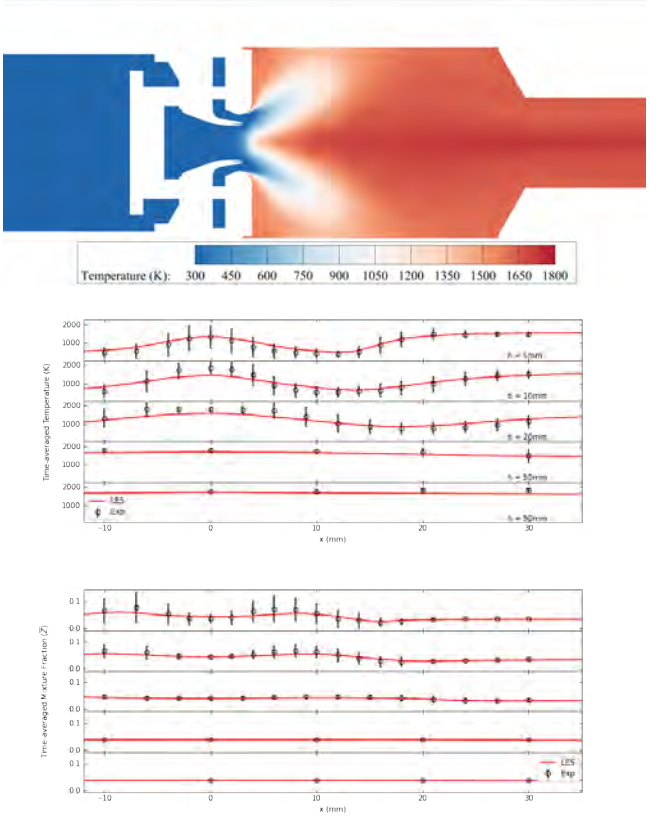

Figure 8. Time-Averaged temperature and mixture fraction field for flame A

premixed flame conditions. Examining the correlation between mixture fraction and temperature in the simulation vs. experimental spectroscopy measurements can give quantitative insight into the consistency between the experimental configuration and the simulation's combustion model. This correlation of these for Flame A is shown in Fig. 9. The LES values are Favre-filtered, while the experimental points are single-shot measurements. Because of this, generally, the experimental data points can be expected to exhibit higher temperature values compared to the CFD. There are many points at low temperature at various mixture fractions for both flame A and B, which indicates a partially premixed flame. Despite this, flame A shows relatively strong agreement. The higher temperature clusters (0-2 and 21-27mm) represent the IRZ and ORZ, respectively, and are regions that are a majority fully reacted products.

Unsteady PIV Comparison

While the simulation of the averaged quantities is relevant for design point characterization, in the context of thermo-acoustic instability, it gives little insight into the underlying mechanisms. For the DLR combustor, unsteady characterization was achieved using a high-speed kilohertz PIV window. By taking specific points in the flow field, the key hydrodynamic and acoustic frequencies can be isolated. These measurements were conducted at 10 kHz for Flame A. This region is shown in figure 10 and is centered at the nozzle exit to examine the recirculation zones and shear layers present. These three points of interest are the swirling

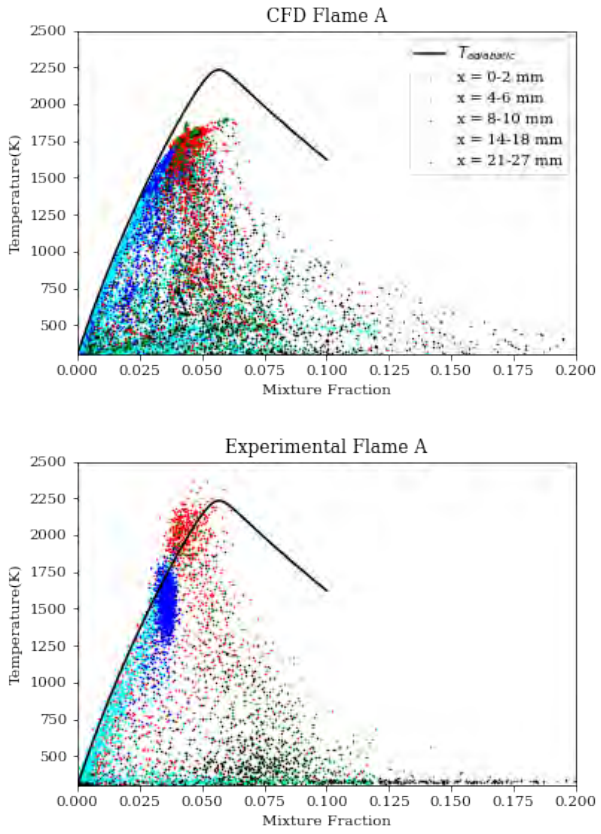

Figure 9. Temperature vs mixture fraction scatter plots for experimental and CFD at $h = 5$mm

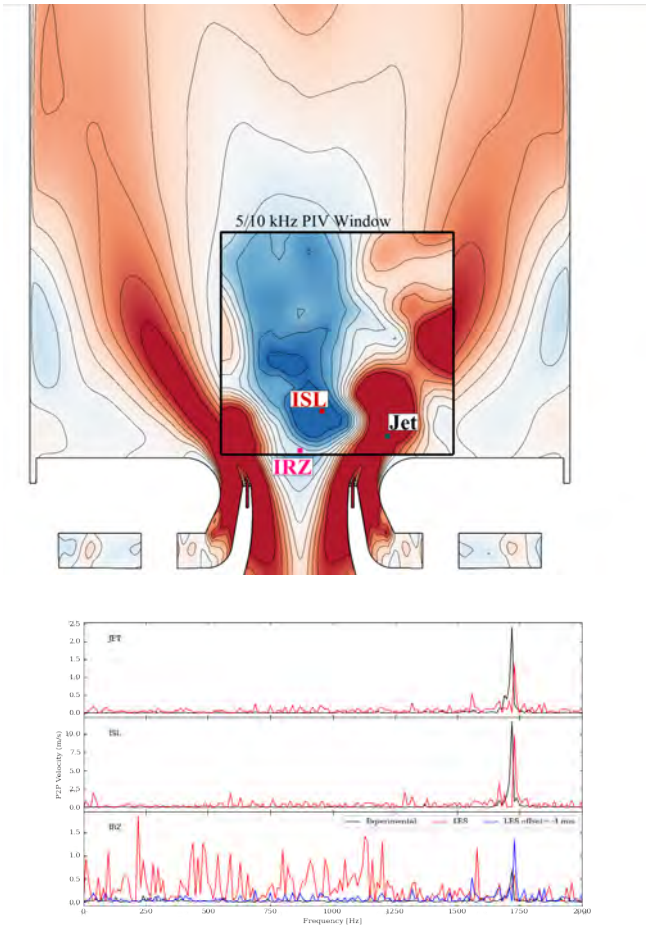

Figure 10. Schematic of kHz PIV window with points of interest label (Top) power spectrum of axial velocity comparison of points of interest (Bottom)

JET, the inner shear layer (ISL), and the inner recirculation zone (IRZ).

Experimental Comparison with PIV

While the simulation of the averaged quantities is relevant for design point characterization, in the context of thermo-acoustic instability, it gives little insight into the underlying mechanisms. For the DLR combustor, unsteady characterization was achieved using a high-speed kilohertz PIV window. By taking specific points in the flow field, the critical hydrodynamic and acoustic frequencies can be isolated. These measurements were conducted at 10 kHz for Flame A. This region is shown in figure 10 and is centered at the nozzle exit to examine the recirculation zones and shear layers present. These three points of interest are the swirling JET, the inner shear layer (ISL), and the inner recirculation zone (IRZ).

Dynamic Mode Decomposition

While single point probes can directly compare experimental results, the nature of simulation data allows more comprehensive methods to be used. In particular, when trying to predict the characteristic frequencies of large-scale structures, the resulting spectrum can be extremely sensitive to the probe location. Modal decompositions are a family of methods that can gain additional insight by leveraging spatial data. Boxx (59) calculated proper orthogonal decomposed(POD) modes which were able to visualize the PVC structure. It was later shown (60) that for systems exhibiting combustion instability, Dynamic Mode Decomposition (DMD) (61) can create more temporally consistent mode shapes, which can both identify hydrodynamic and acoustic features. DMD extracts more physical representations of complex spatio-temporal structures than POD by constraining the temporal modes to discrete frequencies. Details of this methodology for sampling choice and formulation can be found in previous works (60; 62) but is summarized here.

The field data $\mathbf{a}_i \in \mathbb{R}^M$ corresponding to time instants $1 \leq i \leq N$ is assembled into the following matrices

$$\mathbf{A}_1 = \begin{bmatrix} \mathbf{a}_1 & \mathbf{a}_2 & \dots & \mathbf{a}_{N-1} \end{bmatrix} \in \mathbb{R}^{M \times N-1} ;$$
$$\mathbf{A}_2 = \begin{bmatrix} \mathbf{a}_2 & \mathbf{a}_3 & \dots & \mathbf{a}_{N} \end{bmatrix} \in \mathbb{R}^{M \times N-1}$$

which are related to each other via the time advancement matrix $\mathbf{S}$ in the form $\mathbf{A}_2 = \mathbf{A}_1\mathbf{S}$. Following (63), we perform a Singular Value Decomposition $\mathbf{A}_1 = \mathbf{U}\mathbf{\Sigma}\mathbf{V}^T$. In a similarity form, $\tilde{\mathbf{S}} = \mathbf{U}\mathbf{A}_2\mathbf{V}\mathbf{\Sigma}^{-1}$ is related to $\mathbf{S}$ in the form $\tilde{\mathbf{S}} = \tilde{\mathbf{T}}\tilde{\mathbf{\Delta}}\tilde{\mathbf{T}}^{-1}$, and the spatial modes (DMD modes) are constructed as $\mathbf{\Phi} = \mathbf{U}\tilde{\mathbf{T}}$. Using general decomposition form we form the temporal modes $\mathbf{Y}$ as $\mathbf{Y}^{T^{-1}} = \mathbf{V}\mathbf{\Sigma}^{-1}\tilde{\mathbf{T}}$, and thus the response corresponding to each mode is $R_i = \psi_i \mathbf{y}_i^T$.

Applying this methodology to the simulation data, one can visualize the complex 3D hydrodynamic features such as the PVC more effectively. Further, this analysis is more

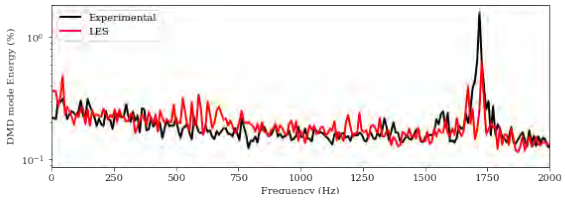

Figure 11. DMD spectrum of axial velocity of the PIV data compared with interpolated CFD data for Flame A

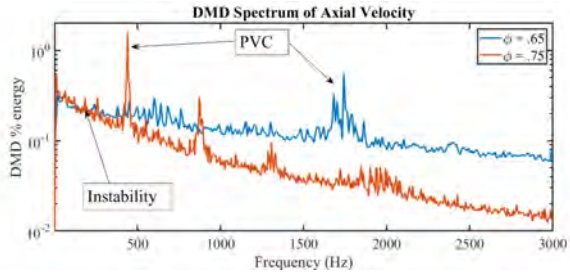

Figure 12. DMD spectrum of axial velocity full CFD three dimensional flow field for flame A

robust to discrepancies in probe location as it is applied to the entire spatial field. Applying this core methodology described by Huang et al. (64) additional prepossessing using singular value truncation and total-least squares (TLS) preconditioning as described by Kutz et al. (65). This prepossessing is significant in applying this combustor as the instability amplitudes are extremely small (.1% of mean pressure) and can be easily diluted by noise, especially with the statistical limits imposed by the CFD run time.

Decomposition of high-frequency PIV window

DMD is first conducted on the small high-frequency PIV window described earlier and compared to the LES data set interpolated onto an identical mesh to compare the experimental and computational decompositions directly. The same sampling rate and the total number of snapshots used corresponded to the available simulation data. The resulting spectra are shown in Fig. 11. Similar to the point analysis, good agreement was found between the computation and experimental results. The PVC frequency is well identified in both the interpolated LES and experimental data sets. Otherwise, the LES contains a slightly higher energy level across the overall frequency space. This is suspected to be due to the reflection of acoustic energy from the pressure outlet boundary condition.

Full 3D Data

An identical methodology, as used on the PIV fields, is applied to the 3D field data for axial velocity and pressure, as shown in Fig. 12. The axial velocity spectrum shows many of the same structures as the 2D experimental DMD. The flame A PVC is observable at 1700 and is visualized in Fig. 13. The vortical corkscrew shape structure can be observed much more clearly than in the raw CFD field.

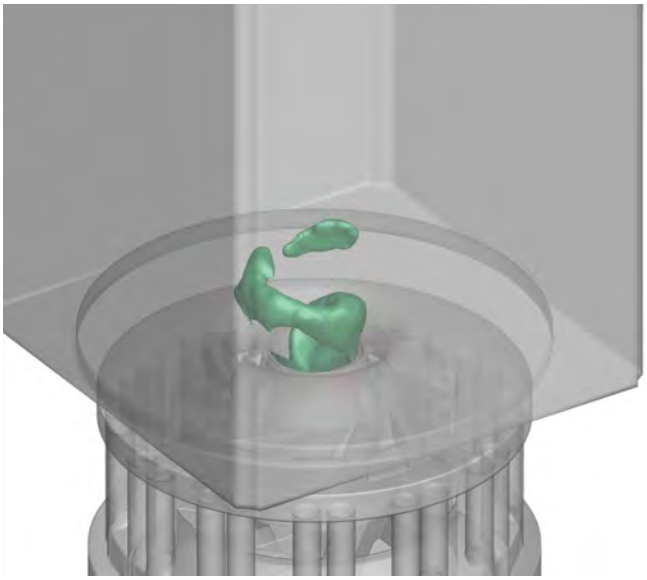

Figure 13. PVC(1750 Hz) DMD mode visualizations for flame A

Reduced-Order Modeling (ROM)

Projection-based ROMs seek a low-dimensional representation of a dynamical system state and a projection of the governing equations onto the low-dimensional space to reduce the computational cost of numerical solutions for high-dimensional systems. To describe this approach, we describe a general non-linear dynamical system ODE,

$$\frac{d\mathbf{q}}{dt} = \mathbf{R}(\mathbf{q}, t), \quad \mathbf{q}(t_0) = \mathbf{q}_0, \tag{1}$$

where $\mathbf{q} \in \mathbb{R}^M$ represents the system solution, and $\mathbf{R}$ represents the non-linear function which describes the spatially discretized terms in the original governing PDE. For this system, the dimension of the system M can be extremely large ($N_{vars} \times N_{cells}$): 6.2×10^7 for this problem. Repeatedly solving this system for different operating conditions is prohibitively expensive and requires extensive computing resources. The ultimate goal of model order reduction techniques is to reduce the dimension of Eqn. 1 without significantly compromising the accuracy of the underlying dynamics.

To begin this process, the state vector is approximated by the transformation

$$\mathbf{q}(t) \approx \overline{\mathbf{q}} + \mathbf{P}\mathbf{V}\hat{\mathbf{q}}(t),$$

where $\overline{\mathbf{q}}$ represents a constant reference state, $\mathbf{V} \in \mathbb{R}^{M \times k}$ is the *trial* basis composed of k linearly independent vectors, $\mathbf{P}$ is a matrix representing the normalization of different variables in the state $\mathbf{q}$, and $\hat{\mathbf{q}}(t)$ represent the modal coefficients describing the linear combination of the trial basis vectors describing the approximate state of $\mathbf{q}$.

The approximate state can be directly substituted into the governing (Eqn. 1) to obtain

$$\frac{d\hat{\mathbf{q}}}{dt} = \mathbf{R}(\overline{\mathbf{q}} + \mathbf{P}\mathbf{V}\hat{\mathbf{q}}, t), \quad \hat{\mathbf{q}}_0 = \hat{\mathbf{q}}(t_0).$$

Recognizing that $\mathbf{P}$, $\overline{\mathbf{q}}$, and $\mathbf{V}$ are constant in time, we are able to simplify this to

$$\mathbf{V}\frac{d\hat{\mathbf{q}}}{dt} = \mathbf{P}^{-1}\mathbf{R}(\hat{\mathbf{q}}, t)$$

Here we observe that $\mathbf{V}\frac{d\hat{\mathbf{q}}}{dt} \in \mathbb{R}^M$ and no dimension reduction has occurred. Finally, we project the system onto a low-dimensional *test space*, via the *test basis* $\mathbf{W} \in \mathbb{R}^{M\times k}$. Like the trail basis $\mathbf{V}$, the test basis $\mathbf{W}$ is a set of k linearly independent vectors. This forms

$$\mathbf{W}^T\mathbf{V}\frac{d\hat{\mathbf{q}}}{dt} = \mathbf{W}^T\mathbf{P}^{-1}\mathbf{R}(\hat{\mathbf{q}}, t), \tag{2}$$

where an ODE system of reduced dimension k has been achieved. This reduced system can be advanced using standard time-integration schemes (explicit or implicit). Clearly, the choice of the bases $\mathbf{W}$ and $\mathbf{V}$ are critical in the success of the ROM. Typically the trial basis $\mathbf{V}$ is computed utilizing the proper orthogonal decomposition (POD) of the data-set trajectory. In the situation of where the trial basis equals the test basis $\mathbf{W} = \mathbf{V}$ Eq. 2 simplifies to

$$\frac{d\hat{\mathbf{q}}}{dt} = \mathbf{V}^T\mathbf{P}\mathbf{R}(\tilde{\hat{\mathbf{q}}}, t)$$

and is referred to as a Galerkin projection.

Another method seeks to formulate the test basis $\mathbf{W}$ so that the fully-discrete FOM residual $\mathbf{r}$ is minimized, which is referred to as the least-squares Petrov-Galerkin (LSPG) projection (42). For a generic linear multi-step method with s steps the $\mathbf{r}$ can be given as

$$\mathbf{r}^n = a_0\mathbf{q}^n + \sum_{i=1}^{s} a_i\mathbf{q}^{n-i} - \Delta\beta_0\mathbf{R}(\mathbf{q}^n, t) - \Delta t\sum_{i=1}^{s}\beta_i\mathbf{R}(\mathbf{q}^{n-i}, t^{n-i}),$$

where β_0 is dependent on the time integration scheme.

The minimization problem for solving the ROM at time instance n can be posed as

$$\hat{\mathbf{q}}^n = \underset{\hat{\mathbf{q}}^n\in\mathbb{R}^k}{\text{argmin}}||\mathbf{P}^{-1}\mathbf{r}(\overline{\mathbf{q}} + \mathbf{P}\mathbf{V}\mathbf{a}, t^n)||_2^2.$$

This produces a test basis of the form

$$\mathbf{W}^n = \mathbf{P}^{-1}\frac{\partial\mathbf{r}^n}{\partial\hat{\mathbf{q}}^n}\mathbf{P}\mathbf{V}. \tag{3}$$

For a linear multi-step method this results in a test basis of the form

$$\mathbf{W}^n = \mathbf{P}(\mathbf{I} - \Delta t\beta_0\frac{\partial\mathbf{r}^n}{\partial\mathbf{q}^n})\mathbf{P}^{-1}\mathbf{V}.$$

Notably for an explicit integrator $\mathbf{W}^n = \mathbf{V}$ reducing to the Galerkin projection. This method has been successfully used for a variety of non-reacting flow applications.

Both of these methods face challenges (45) in their application to reacting flow problems. In particular both methods have shown to exhibit non physical oscillations and generally suffer from stability problems associated with the stiffness of the problem, and in handling the high gradients present in flames (45). Further details on the stability characteristics of Galerkin and LSPG methods can be found in Huang et al. (43).

A more recent variant of the LSPG method of ROM formulations is the structure preserving least-squares variable transformation(SP-LSVT). The SP-LSVT formulation uses a combination of approaches to improve the robustness of the ROM. The variable transformation allows for symmetrization (and hence global linear stability) while maintaining discrete consistency and structure preservation. Local stability is enhanced using physical limiters. Refs. (43) and (66) provides additional details of the SP-LVST methodology for performance and hyper-reduction achievable on 3D problems. SP-LSVT allows one to represent the system state as a function of primitive variables $\mathbf{q}_p$. An additional normalization matrix $\mathbf{H}$ is applied to the primitive variables to further improves the conditioning of the system as $\mathbf{q}_p(t) \approx \overline{\mathbf{q}}_p + \mathbf{H}\mathbf{V}_p\hat{\mathbf{q}}_p(t)$. If a dual-time stepping algorithm is used with k denoting the pseudo time iterations (with physical time Δt and pseudo time $\Delta\tau$, the SP-LSVT yields the following update equation:

$$(\mathbf{W}_p^{k-1})^T(\frac{\Delta t}{\Delta\tau}\Gamma_p^{k-1})(\hat{\mathbf{q}}_p^k - \hat{\mathbf{q}}_p^{k-1}) + (\mathbf{W}_p^{k-1})^T\mathbf{r}(\tilde{\mathbf{q}}_p^{k-1}) = 0,$$

with a test basis

$$\mathbf{W}_p^k = \mathbf{P}\left[(\frac{\Delta t}{\Delta\tau} + 1)\Gamma^{k-1} - \Delta t\beta_0 J^k\Gamma^{k-1}\right]\mathbf{H}\mathbf{V}_p,$$

where $J = \frac{\partial\mathbf{R}}{\partial\mathbf{q}_p}$, and $\Gamma = \frac{\partial\mathbf{q}}{\partial\mathbf{q}_p}$.

Basis Generation

We now describe the procedure for generation of the desired trial basis $\mathbf{V}$. For the reacting flow problems exhibited in this work, the primitive solution vector is organized as

$$\mathbf{q}_p = \begin{bmatrix}\mathbf{p} & \mathbf{u} & \mathbf{T} & \mathbf{Z_m} & \mathbf{Z''^2} & \mathbf{C}\end{bmatrix}^T. \tag{4}$$

Each of the N solution snapshots gathered by evolving Eqn. 1 in time are stored as columns of the complete data matrix as shown in Eq. 4,

$$\mathbf{Q} = \begin{bmatrix}\mathbf{q}(t_1) & \mathbf{q}(t_2) & \dots & \mathbf{q}(t_N)\end{bmatrix}.$$

Next, the reference state $\overline{\mathbf{a}}$ (e.g. the initial condition snapshot $\mathbf{a}_0$ or a time-averaged field) is subtracted from each snapshot, and the resulting matrix is normalized by the diagonal matrix $\mathbf{P}$,

$$\mathbf{Q}' = \mathbf{P}(\mathbf{Q} - \overline{\mathbf{q}}\mathbf{1}^T)$$

Choosing the normalization constants in $\mathbf{P}$ such that the variables are scaled to similar orders of magnitude ensures that all variables are considered equally relevant. Choices for computing these normalization constants include the maximum absolute perturbation value and the L2 norm measure described in (45).

The trail basis $\mathbf{V}$ is then formed using proper orthogonal decomposition (POD).

$$\mathbf{V} = \underset{\mathbf{A}\in\mathbb{R}^{N\times k};\mathbf{V}\mathbf{V}^T=\mathbf{I}}{\text{argmin}}||\mathbf{Q}' - \mathbf{A}\mathbf{A}^T\mathbf{Q}'||_2 \tag{5}$$

The solution to this problem is typically computed using the singular value decomposition. When applied to datasets

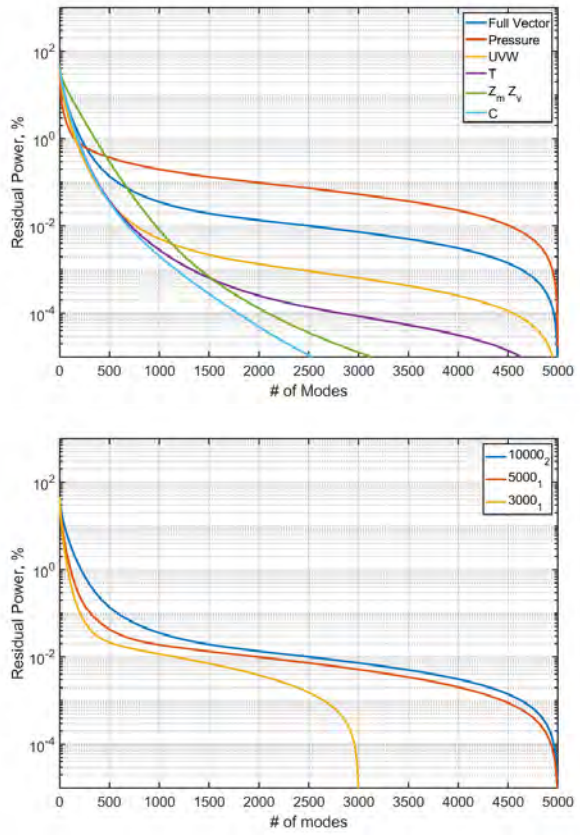

Figure 14. Singular value decay residual for GTMC for various variable groupings for a 5000 snapshot training region (top) and training region lengths (bottom)

of this scale, the associated memory cost can become extremely large, requiring specialized tools. For example, the basis generation for this relatively small time series requires three matrices, each of size $(2.9 \times 10^8) \times (10^4)$ matrices to be allocated in memory. To facilitate this In conjunction with the ROM module added to the GEMS solver, a distributed memory linear algebra tool, leveraging ScaLAPACK and MPI-IO routines, has been developed to generate these basis sets for ROM usage and modal analysis as used for the DMD analysis.

The singular values quantitatively describe the cumulative energy content in the spatial modes. This decay is quantified based on the residual power given by

$$\text{Residual Power } \%(n) = \left(1 - \frac{\sum_{i=1}^{i=n} \sigma_i^2}{\sum \sigma_i^2}\right) \times 100\%. \quad (6)$$

However, as seen for the GTMC dataset(Fig. 14) a) there is no clear cut-off, and b) a significant amount of modes is required to resolve a significant portion of the energy. Further, these facts are seen to worsen as the training region is extended. Taken together, this presents a significant challenge for ROMs.

Reduced-Order Modeling (ROM) Results

Initially, the projection-based intrusive ROM method of the LSPG ROM is applied to the Flame A configuration. The static trial basis is generated over a time period of 5 ms. This corresponds to roughly two flow-through periods, roughly three acoustic periods, and 10 PVC cycles. These runs proved to be unsuccessful as even within the training region they suffered from numerical instability and deviated significantly from the FOM dataset (Fig. 15). The SP-LVST method improves significantly in terms of stability and is able to fully reconstruct the training region and advance beyond it. The ROM performance is assessed using unsteady field comparisons at two representative time instances as shown in Fig. 15. It can immediately be observed that the overall dynamics within the basis generation region is well-captured. However, regardless of the number of modes used, the prediction shows significant deviation beyond the training region as seen in the smearing and non-physical character of the unsteady field.

Fig. 16 compares the time traces of pressure and temperature at locations highlighted in Fig. 15 The improvement of the SP-LVST method over the classical LSPG method is observed within the training region. Even with the relatively small number of modes, the method represents the unsteady dynamics well in the training region, but errors accumulate, and a considerable deviation develops in future state prediction (i.e. beyond the training data).

a priori Projection Error Quantification

While the SP-LSVT offers improved stability, the fundamental limitation is governed by the information lost by projecting on to the reduced basis, referred to as projection error. This shortcoming is immediately apparent in the online ROM runs as they advance beyond the training region The projection error outside the training region varies from problem to problem but can be examined offline to observe the upper limit of any choice of basis projected error. The error of the overall state can be quantified as,

$$\text{Projection Error}(t) = \frac{||\mathbf{q} - \mathbf{V}\mathbf{V}^T\mathbf{q}||_2}{||\mathbf{q}||_2}, \quad (7)$$

with the spatial representation given as

$$\text{Field Error}(x,t) = |\mathbf{q} - \mathbf{V}\mathbf{V}^T\mathbf{q}| \quad (8)$$

These metrics are applied to the static basis trained over 5000 snapshots representing 5 ms. The results are shown in Fig. 17. It is immediately apparent that the projection error within the training region is significantly improved with increased dimension. Even with this improvement, outside the training region, the error significantly increases and is insensitive to the variations in the number of modes used. Additionally, even with significant increases in the training region, the projected error reaches the same level as even smaller training regions. This can be visualized in the field error (Fig. 19 as the maximum error in temperature is less than 100 K. However, when projecting a snapshot beyond the training data, we see large deviations with errors up to 1400 K. This represents a significant limitation of using linear static basis in a highly chaotic flow with multi-scale advective transport.

Ultimately the projection error represents the best possible performance of a projection-based ROM using the corresponding basis. The Kolmogorov N-width (67), describes the worst-case error of a projection onto the best possible static linear subspace. For this flow, the slow

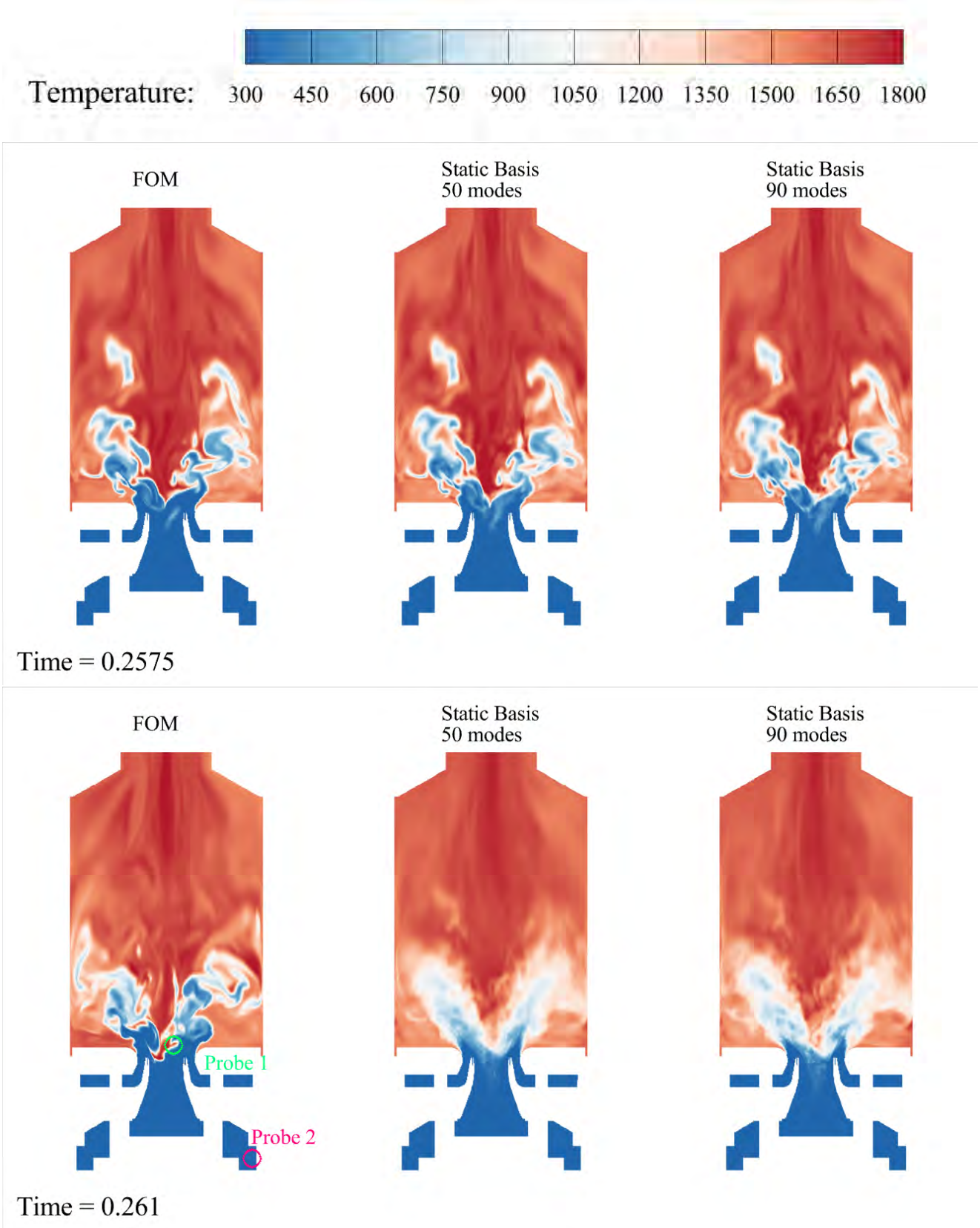

Figure 15. Instantaneous online ROM fields at .5(Top) and 1.2(Bottom) of total training time with Fig. 16 locations highlighted

decay of the singular values signifies a slow decay of the Kolmogorov N-width. Possible approaches that can mitigate this issue include adaptive basis methods (68) and non-linear manifolds (35). However, these techniques are in development, and have not been applied extensively even in 2D non-reacting compressible flow problems.

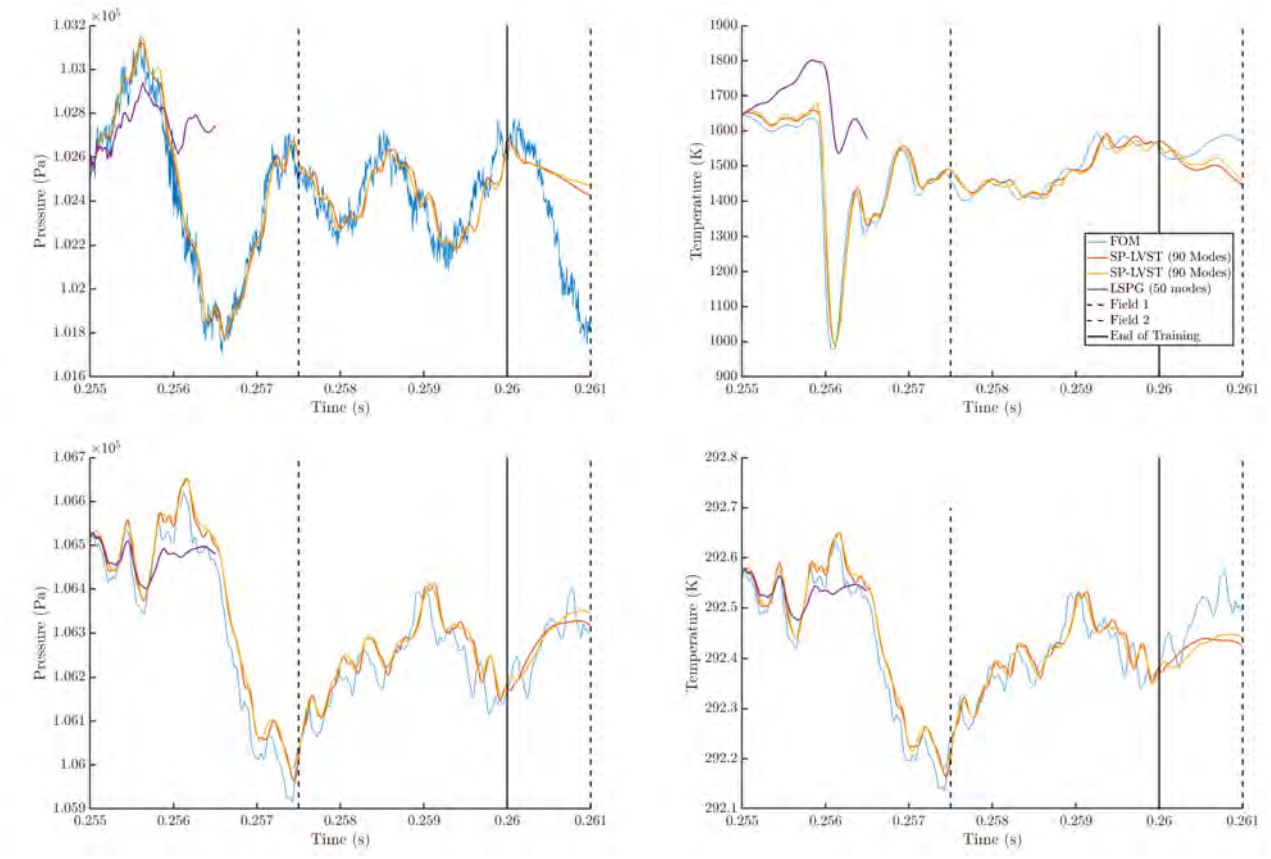

Figure 16. Pressure and Temperature Probes within Flame Front(Top) and Plenum(Bottom) for various Static Basis Choices

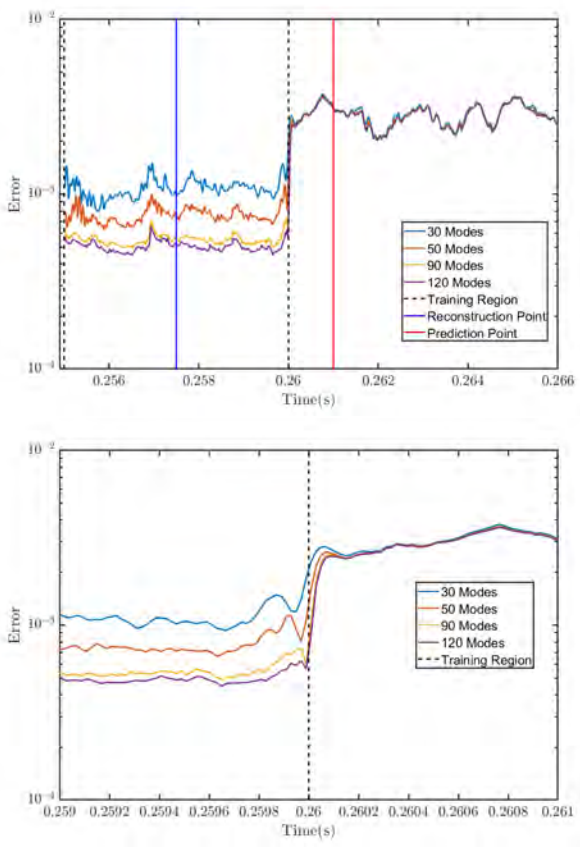

Figure 17. Static Basis Projection error for various mode counts for 5 ms training window (left) and zoomed close to end of Training (right)

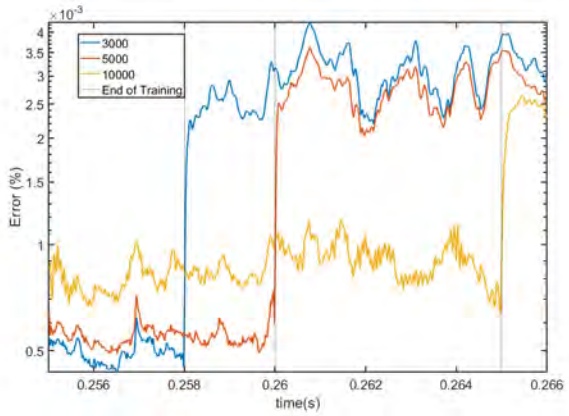

Figure 18. Static Basis Projection Error for 90 modes computed for various training lengths

Conclusions

A reacting large-eddy simulation (LES) of a methane-air dual-swirl gas turbine model combustor (GTMC) is performed using a flamelet-based approach. The simulation is validated with experimental measurements and shows excellent agreement, including accurate prediction of the steady flow features, the recirculation bubble and overall flame shape, and unsteady features. These validations are supplemented via Dynamic mode decomposition (DMD). The DMD analysis reveals the dynamics of the precessing vortex core, and allows for a quantitative comparison of the frequency spectrum of the entire PIV window.

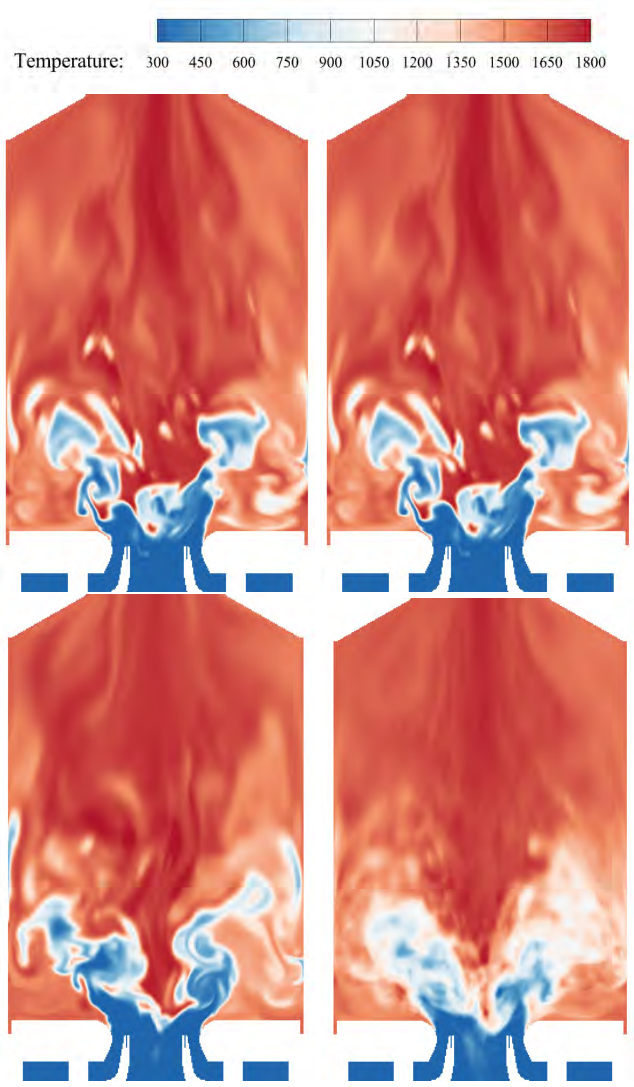

Figure 19. Full-Order Model (Left) Temperature Field compared with a priori Static Basis 90 mode Projection (Right) at t=.275(Top) and t=.261(Bottom)

Snapshots from this simulation are used to develop a reduced dimensional linear subspace using proper orthogonal decomposition. This basis is first used with the well-known least-squares Petrov Galerkin(LSPG). Even within the training region, this method suffers from significant numerical stability issues. Following this, the same basis is used in the structure-preserving least-squares variable transformation. This method shows significantly better stability and is able to replicate the training data successfully. However, the SP-LSVT technique develops significant error in future state prediction, which is a direct consequence of the high projection error.

In summary, the linear manifold-based SP-LVST method improves the overall performance of the ROM, but is still limited by the choice of basis. In addition to the full-order modeling and reduced-order method development, for problems of this scale, a robust parallelized tool chain is required to facilitate this work. It is noted that formal projection-based reduced-order modeling of a problem of this scale and complexity remains a grand challenge. This work represents initial steps towards the development of a robust reduced-order modeling framework for gas turbine combustion dynamics. Continuing work is being dedicated towards the use of adaptive basis to overcome the limitation of a static linear manifold.

Acknowledgements The authors would like to acknowledge the Department of Defense High Performance Computing Modernization Program (HPCMP) and University of Michigan Advanced Research and Computing Technology Services (ARC-TS) for providing the computing resources. The authors would also like to thank James Driscoll for providing the experimental geometry, as well as Mirko Gamba, Wolfgang Meier, Nedunchezhian Swaminathan, and Zhu Chen for facilitating, providing, and assisting with the experimental data set.

Funding Statement This work is supported under under NSF grant CMMI 1634709, “A Diagnostic Modeling Methodology for Dual Retrospective Cost Adaptive Control of Complex Systems.”

Declaration of Interests The authors declare no conflict of interest.

Data Availability Statement Simulation data and computational meshes can be requested from the corresponding author. The experimental data can be requested through the German Aerospace Center(DLR).

Ethical Standards The research meets all ethical guidelines, including adherence to the legal requirements of the study country.

References

[1] Meier W, Duan XR and Weigand P. Reaction zone structures and mixing characteristics of partially premixed swirling CH4/air flames in a gas turbine model combustor. *Proceedings of the Combustion Institute* 2005; 30(1): 835–842. DOI:10.1016/j.proci.2004.08.065. URL http://dx.doi.org/10.1016/j.proci.2004.08.065.

[2] Lieuwen TC and Yang V. *Combustion Instabilities in Gas Turbine Engines: Operational Experience, Fundamental Mechanisms, and Modeling*. American Institute of Aeronautics and Astronautics, Inc., 2010. ISBN 156347669X.

[3] Richards GA, Straub DL and Robey EH. Passive Control of Combustion Dynamics in Stationary Gas Turbines. *Journal of Propulsion and Power* 2003; 19(5): 795–810. DOI:10.2514/2.6195.

[4] Zhao D, Lu Z, Zhao H et al. A review of active control approaches in stabilizing combustion systems in aerospace industry. *Progress in Aerospace Sciences* 2018; 97(April 2017): 35–60. DOI:10.1016/j.paerosci.2018.01.002.

[5] Mallard E. Recherches experimentales et theoriques sur la combustion des melanges gaseux explosifs. *Ann mines* 1883; 8(4): 274–568.

[6] Strutt JW and Rayleigh B. The explanation of certain acoustical phenomena. *Nature* 1878; 18: 319–321.

[7] Huang Y and Yang V. Unsteady Flow Evolution and Flame Dynamics in. In *Proceeding of Third International Symposium on Turbulent and Shear Flow Phenomena*. pp. 1–6.

[8] Huang Y and Yang V. Effect of swirl on combustion dynamics in a lean-premixed swirl-stabilized combustor. *Proceedings of the Combustion Institute* 2005; 30 II(2): 1775–1782. DOI:10.

1016/j.proci.2004.08.237. URL http://dx.doi.org/10.1016/j.proci.2004.08.237.

[9] Huang Y, Sung HG, Hsieh SY et al. Large-Eddy Simulation of Combustion Dynamics of Lean-Premixed Swirl-Stabilized Combustor. *Journal of Propulsion and Power* 2003; 19(5): 782–794. DOI:10.2514/2.6194.

[10] Broda JC, Seo S, Santoro RJ et al. An experimental study of combustion dynamics of a premixed swirl injector. *Symposium (International) on Combustion* 1998; 27(2): 1849–1856. DOI:10.1016/S0082-0784(98)80027-1.

[11] See YC and Ihme M. Large eddy simulation of a partially-premixed gas turbine model combustor. *Proceedings of the Combustion Institute* 2015; 35(2): 1225–1234. DOI:10.1016/j.proci.2014.08.006. URL http://dx.doi.org/10.1016/j.proci.2014.08.006.

[12] Huang C, Gejji R, Anderson W et al. Combustion Dynamics in a Single-Element Lean Direct Injection Gas Turbine Combustor. *Combustion Science and Technology* 2019; 0(0): 1–28. DOI:10.1080/00102202.2019.1646732. URL https://doi.org/10.1080/00102202.2019.1646732.

[13] Poinsot T. Prediction and control of combustion instabilities in real engines. *Proceedings of the Combustion Institute* 2017; 36(1): 1–28. DOI:10.1016/j.proci.2016.05.007. URL http://dx.doi.org/10.1016/j.proci.2016.05.007.

[14] Stöhr M, Boxx I, Carter CD et al. Experimental study of vortex-flame interaction in a gas turbine model combustor. *Combustion and Flame* 2012; 159(8): 2636–2649. DOI:10.1016/j.combustflame.2012.03.020.

[15] Stöhr M, Yin Z and Meier W. Interaction between velocity fluctuations and equivalence ratio fluctuations during thermoacoustic oscillations in a partially premixed swirl combustor. *Proceedings of the Combustion Institute* 2017; 36(3): 3907–3915. DOI:10.1016/j.proci.2016.06.084.

[16] Weigand P, Meier W, Duan XR et al. Laser diagnostic study of the mechanism of a periodic combustion instability in a gas turbine model combustor. *Flow, Turbulence and Combustion* 2005; 75(1-4): 275–292. DOI:10.1007/s10494-005-8585-2.

[17] Weigand P, Meier W, Duan X et al. Investigations of swirl flames in a gas turbine model combustor. *Combustion and Flame* 2006; 144(1-2): 205–224. DOI:10.1016/j.combustflame.2005.07.010. URL https://linkinghub.elsevier.com/retrieve/pii/S0010218005001963.

[18] Arndt CM, Severin M, Dem C et al. Experimental analysis of thermo-acoustic instabilities in a generic gas turbine combustor by phase-correlated PIV, chemiluminescence, and laser Raman scattering measurements. *Experiments in Fluids* 2015; 56(4): 1–23. DOI:10.1007/s00348-015-1929-3. URL http://dx.doi.org/10.1007/s00348-015-1929-3.

[19] Arndt CM, Steinberg AM and Meier W. Flame Extinction and Re-Ignition in a Swirl Stabilized Prevaporized Liquid Fuel Flame Close to Lean Blow-Out. In *AIAA Scitech 2020 Forum*. January, pp. 1–10. DOI:10.2514/6.2020-1879.

[20] Kraus C, Selle L and Poinsot T. Coupling heat transfer and large eddy simulation for combustion instability prediction in a swirl burner. *Combustion and Flame* 2018; 191: 239–251. DOI:10.1016/j.combustflame.2018.01.007.

[21] Steinberg AM, Boxx I, Stöhr M et al. Effects of flow structure dynamics on thermoacoustic instabilities in swirl-stabilized combustion. *AIAA Journal* 2012; 50(4): 952–967. DOI:10.2514/1.J051466.

[22] Stöhr M and Meier W. Investigation of a Periodic Combustion Instability in a Swirl Burner Using Phase-Resolved PIV. *Proceedings of the European Combustion Meeting 2007* 2007; (March): 1–6.

[23] Stöhr M, Arndt CM and Meier W. Transient effects of fuel-air mixing in a partially-premixed turbulent swirl flame. *Proceedings of the Combustion Institute* 2015; 35(3): 3327–3335. DOI:10.1016/j.proci.2014.06.095.

[24] Allison PM, Driscoll JF and Ihme M. Acoustic characterization of a partially-premixed gas turbine model combustor: Syngas and hydrocarbon fuel comparisons. *Proceedings of the Combustion Institute* 2013; 34(2): 3145–3153. DOI:10.1016/j.proci.2012.06.157. URL http://dx.doi.org/10.1016/j.proci.2012.06.157.

[25] Allison PM. *Experimental Characterization of Combustion Instabilities and Flow-Flame Dynamics in a Partially-Premixed Gas Turbine Model Combustor*. PhD Thesis, University of Michigan, 2013.

[26] Widenhorn A, Noll B and Aigner M. Numerical characterisation of a gas turbine model combustor applying scale-adaptive simulation. *Proceedings of the ASME Turbo Expo* 2009; 2: 11–23. DOI:10.1115/GT2009-59038.

[27] Koo H, Hassanaly M, Raman V et al. Large-Eddy Simulation of Soot Formation in a Model Gas Turbine Combustor. *Journal of Engineering for Gas Turbines and Power* 2017; 139(3): 1–9. DOI:10.1115/1.4034448.

[28] Chen ZX, Langella I, Swaminathan N et al. Large Eddy Simulation of a dual swirl gas turbine combustor: Flame/flow structures and stabilisation under thermoacoustically stable and unstable conditions. *Combustion and Flame* 2019; 203: 279–300. DOI:10.1016/j.combustflame.2019.02.013. URL https://doi.org/10.1016/j.combustflame.2019.02.013.

[29] Chen ZX and Swaminathan N. Influence of fuel plenum on thermoacoustic oscillations inside a swirl combustor. *Fuel* 2020; 275(February): 117868. DOI:10.1016/j.fuel.2020.117868. URL https://doi.org/10.1016/j.fuel.2020.117868.

[30] Lumley JL and Poje A. Low-dimensional models for flows with density fluctuations. *Physics of Fluids* 1997; 9(7): 2023–2031. DOI:10.1063/1.869321.

[31] Graham WR, Peraire J and Tang KY. Optimal control of vortex shedding using low-order models. Part II - Model-based control. *International Journal for Numerical Methods in Engineering* 1999; 44(7): 973–990. DOI:10.1002/(SICI)1097-0207(19990310)44:7⟨973::AID-NME538⟩3.0.CO;2-F.

[32] Lucia DJ and Beran PS. Projection methods for reduced order models of compressible flows. *Journal of Computational Physics* 2003; 188(1): 252–280. DOI:10.1016/S0021-9991(03)00166-9.

[33] Rempfer D. On low-dimensional Galerkin models for fluid flow. *Theoretical and Computational Fluid Dynamics* 2000; 14(2): 75–88. DOI:10.1007/s001620050131.

[34] Bergmann M, Bruneau CH and Iollo A. Enablers for robust POD models. *Journal of Computational Physics* 2009; 228(2): 516–538. DOI:10.1016/j.jcp.2008.09.024. URL http://dx.doi.org/10.1016/j.jcp.2008.09.024.

[35] Lee K and Carlberg KT. Model reduction of dynamical systems on nonlinear manifolds using deep convolutional autoencoders. *Journal of Computational Physics* 2020; 404: 108973. DOI:10.1016/j.jcp.2019.108973. URL https://doi.org/10.1016/j.jcp.2019.108973.

[36] Rowley CW. Model reduction for fluids, using balanced proper orthogonal decomposition. *International Journal of Bifurcation and Chaos in Applied Sciences and Engineering* 2005; 15(3): 997–1013. DOI:10.1142/S0218127405012429.

[37] Willcox K and Peraire J. Balanced model reduction via the proper orthogonal decomposition. *AIAA Journal* 2002; 40(11): 2323–2330. DOI:10.2514/2.1570.

[38] Rowley CW, Colonius T and Murray RM. Model reduction for compressible flows using POD and Galerkin projection. *Physica D: Nonlinear Phenomena* 2004; 189(1-2): 115–129. DOI:10.1016/j.physd.2003.03.001.

[39] Parish EJ, Wentland CR and Duraisamy K. The Adjoint Petrov–Galerkin method for non-linear model reduction. *Computer Methods in Applied Mechanics and Engineering* 2020; 365: 112991. DOI:10.1016/j.cma.2020.112991. URL https://doi.org/10.1016/j.cma.2020.112991.

[40] Ahmed SE, Pawar S, San O et al. On closures for reduced order models $-$ A spectrum of first-principle to machine-learned avenues 2021; : 1–34URL http://arxiv.org/abs/2106.14954.

[41] Afkham BM, Ripamonti N, Wang Q et al. Conservative model order reduction for fluid flow. In *Quantification of Uncertainty: Improving Efficiency and Technology*. Springer, 2020. pp. 67–99.

[42] Carlberg K, Charbel BM and Charbel F. Efficient non-linear model reduction via a least-squares Petrov–Galerkin projection and compressive tensor approximations. *INTERNATIONAL JOURNAL FOR NUMERICAL METHODS IN ENGINEERING Int* 2010; (October): 155–181.

[43] Huang C, Wentland CR, Duraisamy K et al. Model Reduction for Multi-Scale Transport Problems using Structure-Preserving Least-Squares Projections with Variable Transformation 2020; (May 2020). URL http://arxiv.org/abs/2011.02072.

[44] Berkooz G, Holmes P and Lumley J. The Proper Orthogonal Decomposition in the Analysis of Turbulent Flows. *Annual Review of Fluid Mechanics* 1993; 25(1): 539–575. DOI:10.1146/annurev.fluid.25.1.539.

[45] Huang C, Duraisamy K and Merkle CL. Challenges in reduced order modeling of reacting flow. *2018 Joint Propulsion Conference* 2018; DOI:10.2514/6.2018-4675.

[46] Nicoud F, Toda HB, Cabrit O et al. Using singular values to build a subgrid-scale model for large eddy simulations. *Physics of Fluids* 2011; 23(8). DOI:10.1063/1.3623274.

[47] Erlebacher G, Hussaini M, Speziale C et al. TOWARD THE LARGE-EDDY SIMULATIONS OF COMPRESSIBLE TURBULENT FLOWS. Technical report, 1987.

[48] Comer AL, Sardeshmukh S, Rankin BA et al. Effects of turbulent combustion closure on grid convergence of bluff body stabilized premixed flame simulations. *AIAA Aerospace Sciences Meeting, 2018* 2018; (210059): 1–19. DOI:10.2514/6.2018-0439.

[49] Comer AL, Huang C, Duraisamy K et al. Sensitivity analysis of bluff body stabilized premixed flame large eddy simulations. *AIAA Scitech 2019 Forum* 2019; (January): 1–17. DOI:10.2514/6.2019-0450.

[50] Pierce CD and Moin P. Progress-variable approach for large-eddy simulation of non-premixed turbulent combustion. *Journal of Fluid Mechanics* 2004; 504(504): 73–97. DOI:10.1017/S0022112004008213.

[51] Pitsch H. FlameMaster: A C++ computer program for 0D combustion and 1D laminar flame calculations. *Cited in* 1998; 81.

[52] Frenklach M, Wang H, Goldenberg M et al. GRI-Mech—an optimized detailed chemical reaction mechanism for methane combustion. *Gas Research Institute topical report, Gas Research Institute, Chicago* 1995; .

[53] McBride BJ. *NASA Glenn coefficients for calculating thermodynamic properties of individual species*. National Aeronautics and Space Administration, John H. Glenn Research Center˜..., 2002.

[54] Wilke CR. A viscosity equation for gas mixtures. *The Journal of Chemical Physics* 1950; 18(4): 517–519. DOI:10.1063/1.1747673.

[55] Mathur S, Tondon PK and Saxena SC. Thermal conductivity of binary, ternary and quaternary mixtures of rare gases. *Molecular Physics* 1967; 12(6): 569–579. DOI:10.1080/00268976700100731.

[56] Li D, Venkateswaran S, Fakhari K et al. Convergence assessment of general fluid equations on unstructured hybrid grids1. *15th AIAA Computational Fluid Dynamics Conference* 2001; (June). DOI:10.2514/6.2001-2557.

[57] P L Roe. Approximate Riemann Solvers, Parameter Vectors, and Difference Schemes. *Journal of Computational Physics* 1981; 43: 357–372.

[58] BARTH T and JESPERSEN D. The design and application of upwind schemes on unstructured meshes 1989; DOI:10.2514/6.1989-366.

[59] Boxx I, Stöhr M, Carter C et al. Temporally resolved planar measurements of transient phenomena in a partially pre-mixed swirl flame in a gas turbine model combustor. *Combustion and Flame* 2010; 157(8): 1510–1525. DOI:10.1016/j.combustflame.2009.12.015. URL http://dx.doi.org/10.1016/j.combustflame.2009.12.015.

[60] Huang C, Anderson WE, Harvazinski ME et al. Analysis of Self-Excited Combustion Instabilities Using Decomposition Techniques. *AIAA Journal* 2016; 54(9): 2791–2807. DOI:10.2514/1.J054557. URL http://arc.aiaa.org/doi/10.2514/1.J054557.

[61] Schmid PJ. Dynamic mode decomposition of numerical and experimental data. *Journal of Fluid Mechanics* 2010; 656: 5–28. DOI:10.1017/S0022112010001217.

[62] Arnold-Medabalimi N, Huang C and Duraisamy K. Data-driven modal decomposition techniques for high-dimensional flow fields. In *Data Analysis for Direct Numerical Simulations of Turbulent Combustion*. Springer, 2020. pp. 135–155.

[63] Schmid PJ. Application of the dynamic mode decomposition to experimental data. *Experiments in Fluids* 2011; 50(4): 1123–1130. DOI:10.1007/s00348-010-0911-3.

[64] Huang C, Gejji RM and Anderson WE. Effects of Physical Modeling on Combustion Instability Predictions in a Single-Element Lean Direct Injection Gas Turbine Combustor. *53rd AIAA Aerospace Sciences Meeting* 2015; (January): 1–16. DOI:10.2514/6.2015-1569. URL http://arc.aiaa.

org/doi/10.2514/6.2015-1569.

[65] Kutz JN, Brunton SL, Brunton BW et al. *Dynamic mode decomposition: data-driven modeling of complex systems*. SIAM, 2016.

[66] Wentland CR, Huang C and Duraisamy K. Investigation of sampling strategies for reduced-order models of rocket combustors. *AIAA Scitech 2021 Forum* 2021; (January): 1–31. DOI:10.2514/6.2021-1371.

[67] Light WA. n-WIDTHS IN APPROXIMATION THEORY (Ergebnisse der Mathematik und ihrer Grenzgebiete 3. Folge, Band 7), 1985.

[68] Peherstorfer B. *Model reduction for transport-dominated problems via online adaptive bases and adaptive sampling*, volume 42. 2020. ISBN 9550171019. DOI:10.1137/19M1257275.